Extreme ultraviolet plasmonics and Cherenkov radiation in silicon

Prashant Shekhar,[1,2,3] 🔾 Sarang Pendharker,[4] 🔾 Harshad Sahasrabudhe,[5] Douglas Vick,[6] Marek Malac,[6] Rajib Rahman,[3] and Zubin Jacob[1,2,3,*]

[1]*Department of Electrical and Computer Engineering, University of Alberta, Edmonton, Alberta T6G 2V4, Canada*
[2]*Birck Nanotechnology Center, Purdue University, West Lafayette, Indiana 47907, USA*
[3]*School of Electrical and Computer Engineering, Purdue University, West Lafayette, Indiana 47907, USA*
[4]*Department of Electronics and Electrical Communication Engineering, Indian Institute of Technology, Kharagpur, West Bengal, India*
[5]*Department of Physics and Astronomy, Purdue University, West Lafayette, Indiana 47907, USA*
[6]*Nanotechnology Research Centre, Nat. Res. Council, Edmonton, Alberta T6G 2M9, Canada*
Corresponding author: zjacob@purdue.edu

Silicon is widely used as the material of choice for semiconductor and insulator applications in nanoelectronics, micro-electro-mechanical systems, solar cells, and on-chip photonics. In stark contrast, in this paper, we explore silicon's metallic properties and show that it can support propagating surface plasmons, collective charge oscillations, in the extreme ultraviolet (EUV) energy regime not possible with other plasmonic materials such as aluminum, silver, or gold. This is fundamentally different from conventional approaches, where doping semiconductors is considered necessary to observe plasmonic behavior. We experimentally map the photonic band structure of EUV surface and bulk plasmons in silicon using momentum-resolved electron energy loss spectroscopy. Our experimental observations are validated by macroscopic electrodynamic electron energy loss theory simulations as well as quantum density functional theory calculations. As an example of exploiting these EUV plasmons for applications, we propose a tunable and broadband thresholdless Cherenkov radiation source in the EUV using silicon plasmonic metamaterials. Our work can pave the way for the field of EUV plasmonics. © 2018 Optical Society of America under the terms of the [OSA Open Access Publishing Agreement](#)

https://doi.org/10.1364/OPTICA.5.001590

1. INTRODUCTION

Silicon is the most widely used material for applications in nanoelectronics [1], photovoltaics [2], micro-electro-mechanical systems [3], and on-chip photonics [4–6]. Its dominance in industry stems from multiple factors, including the possibility of controlling its crystallinity, tailoring of its conducting properties via doping, cost-effectiveness, and availability, as well as its high purity. Although universally known for its insulating and semiconducting properties, the goal of this paper is to explore and exploit silicon's metallic and plasmonic properties, which have remained largely ignored.

The plasmonic properties of a variety of different materials have been explored across the electromagnetic (EM) spectrum [7] [Fig. 1(a)]. This includes plasmons on graphene in the terahertz regime [8], highly doped III-V semiconductors that support plasmons in the infrared [9,10], and the universally used plasmonic materials Ag and Au in the visible [11]. Aluminum has been the most widely explored plasmonic material at ultraviolet (UV) frequencies for applications such as tunable, integratable surface plasmon (SP) sources [12,13], medical assays and biotechnology applications with fluorophores [14], as well as lensing for imaging applications and optical lithography [15]. While aluminum has

shown some promise in the ≈5 eV (248 nm) regime, achieving plasmonic effects at higher energies in the deep ultraviolet (DUV) and extreme ultraviolet (EUV) is an open problem.

In this paper, we show that EUV plasmons supported by silicon can pave the way for EUV waveguides, metamaterials, and devices not possible with conventional plasmonic materials. We study the evolution of the plasmonic behavior in silicon thin films down to 60 nm and probe the photonic band structure of silicon in the EUV up to 5 times past the light line. This is made possible by probing silicon with relativistic electrons using momentum-resolved electron energy loss spectroscopy (k-EELS). Unlike the more traditional spatially resolved electron energy loss techniques [16], in our work, not only the energy but also the momentum dispersion of the EUV plasmonic excitations are mapped. We also show excellent agreement of our experimental results with first principles quantum density functional theory (DFT) calculations as well as macroscopic electrodynamic electron energy loss theory. The silicon surface plasmon polariton (SPP) is shown to have a resonance condition at approximately 11.5 eV (107 nm), more than twice as high in energy as what has been measured with aluminum for applications in the UV. Finally, we propose an EUV radiation source by exploiting the

EUV plasmonic properties of undoped silicon. Our proposed EUV source is tunable and broadband, and uses thresholdless Cherenkov radiation (TCR) in silicon plasmonic hyperbolic metamaterials (HMMs). Our work paves the way for the field of EUV plasmonic devices with silicon.

The energy scales of the SPP for silicon is between $4 \, \text{eV} < E < 11.5 \, \text{ev}$ ($310 \, \text{nm} < \lambda < 107 \, \text{nm}$) while the bulk plasmon (BP) exists at $E = 16 \, \text{eV}$ ($\lambda = 77 \, \text{nm}$). Even though previous work has shed light on the existence of such metallic behavior in bulk silicon [17], it is an open question whether plasmonic behavior would persist for nanoscale structures. In this work, we specifically focus on the thickness evolution of plasmonic behavior in silicon thin films that is in agreement with Drude metallic behavior. This validates that deep subwavelength excitations in the EUV regime are indeed possible for paving the way to EUV plasmonics.

Experimental measurement of the silicon permittivity at high energies [18] agrees strongly with our DFT calculations under the GW approximation [19] [Fig. 1(b)] (see Supplement 1 for details). Silicon's metallic character in the EUV is a result of the unbound nature of its valence electrons. This arises from the weak interband transitions strengths between the valence and conduction band [20,17,21]. In fact, this leads to a nearly freely moving sea of electrons in the valence band that can support SP excitations from the free-charge carrier oscillations. This is in contrast to

(a)

Fig. 1. Plasmonics across the EM spectrum. (a) Measured SP resonance for various materials across the EM spectrum from the terahertz (10^{-2} eV/124 μm) to the EUV (11.5 eV/107 nm); doped semiconductors are limited to the mid-infrared region, whereas transparent conducting oxides have plasmon resonances in the near-infrared. Alternative plasmonic media and conventional materials (Ag, Au) work well in the visible range. Aluminum is the material of choice for UV applications. Plasmonic behavior in the EUV has remained largely ignored. Here, we explore silicon for its EUV plasmonic properties at more than double the energy of aluminum. (b) Experimental (from Palik [18]) and theoretical (DFT) calculations with the GW approximation) of the permittivity of silicon showing its metallic character in the EUV ($\epsilon < 0$ in the 10–16 eV (124–77 nm) regime); (c) electronic band structure of silicon calculated with DFT+GW approximations. Arrows indicate indirect interband transitions that are very weak in the EUV. This results in a sea of unbound electrons in the valence band that leads to silicon's metallic character [20].

the visible region of the spectrum, where prominent interband transitions lead to strongly bound electron-hole pairs between the valence and conduction band, which eliminates its metallic character [20,22].

2. EUV PLASMONS IN SILICON MEASURED WITH *k*-EELS

We measure the EUV plasmonic properties of silicon with relativistic electrons and *k*-EELS in a transmission electron microscope (TEM). Unlike traditional electron energy loss spectroscopy techniques, where only the amount of energy loss is measured, *k*-EELS probes both the energy and momentum transfer of the electron. The information on momentum loss is obtained by measuring the scattering angle (θ) of the electron after passing through the sample [Fig. 2(a) and Supplement 1]. Note the energy and momentum lost by the incident electron corresponds directly to the energy and momentum carried away by the excitations within the sample. Thus, the major advantage of *k*-EELS is the ability to map the photonic/polaritonic band structure and clearly identify photonic excitations such as Cherenkov radiation (CR), waveguide modes, and surface/BPs.

Figures 2(b)–2(d) show the measured photonic band structure as a function of thickness (200, 100, and 60 nm) for free-standing silicon films. The samples are prepared via focused ion beam milling (FIB) and mounted to a TEM grid to create free-standing structures [inset Fig. 2(f) and 2(g)]. The band structure for all three films is measured using *k*-EELS up to an electron scattering angle of $\theta = 30 \, \mu\text{rad}$ ($k_x \approx 0.1 \, \text{nm}^{-1}$) at 300 keV incident energy and probes the deep near field up to 5 times past the light line.

We now explain the physical origin of the three branches seen in the band structure data in Figs. 2(b)–2(d). The dispersionless flatband at 16 eV (77 nm) in all three films is the BP excitation of silicon (ω_p^{Si}). The BP is a longitudinal resonance that is difficult to probe optically and occurs at the point $\epsilon_{\text{Si}} \to 0$ [Fig. 1(b)] well into the EUV. We emphasize that bulk longitudinal plasma oscillations, even for aluminum, occur in this high-energy regime. However, for waveguiding and nanoantenna applications, SPPs are necessary and do not exist in the EUV regime in the widely used plasmonic metals.

The highly dispersive band between $\approx$4–9 eV for the 200 nm film and $\approx$4–11.5 eV (107–310 nm) in the 100 and 60 nm film is the measured SPP excitation of silicon in the EUV. Interestingly, surface excitations are stronger as compared to bulk excitations for thinner films in all electron energy loss spectroscopy measurements due to the Bergrenzungs effect [23,24]. As a result, the SP scattering intensity is large enough in the thinner 100 and 60 nm film to be probed into EUV energies. Interestingly, we note that $\omega_{sp}^{\text{Si}} = \omega_p^{\text{Si}}/\sqrt{2} \approx 11.5 \, \text{eV}$, which is indicative that silicon is a Drude-like metal in the EUV in agreement with DFT calculations. This is in fundamental contrast to the DC semiconducting properties or transparent insulator-like optical properties of silicon at the telecommunication wavelengths.

We immediately note that the measured EUV SPP resonance energy of silicon ($\approx$11.5 eV/107 nm) is more than double of what has been observed with aluminum, the traditional material for high-energy plasmonic applications. Furthermore, Figs. 2(e)–2(g) highlight the highly dispersive nature of the SPP (blueshifting of the peak with increasing scattering angle) for the three silicon films across the untapped 5–11.5 eV range. Note that the
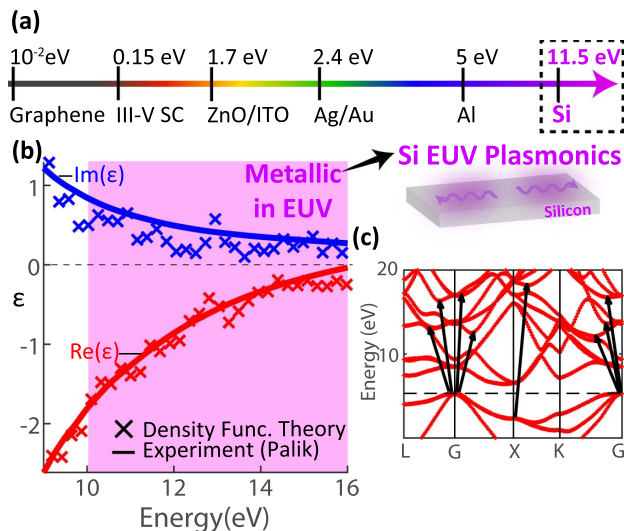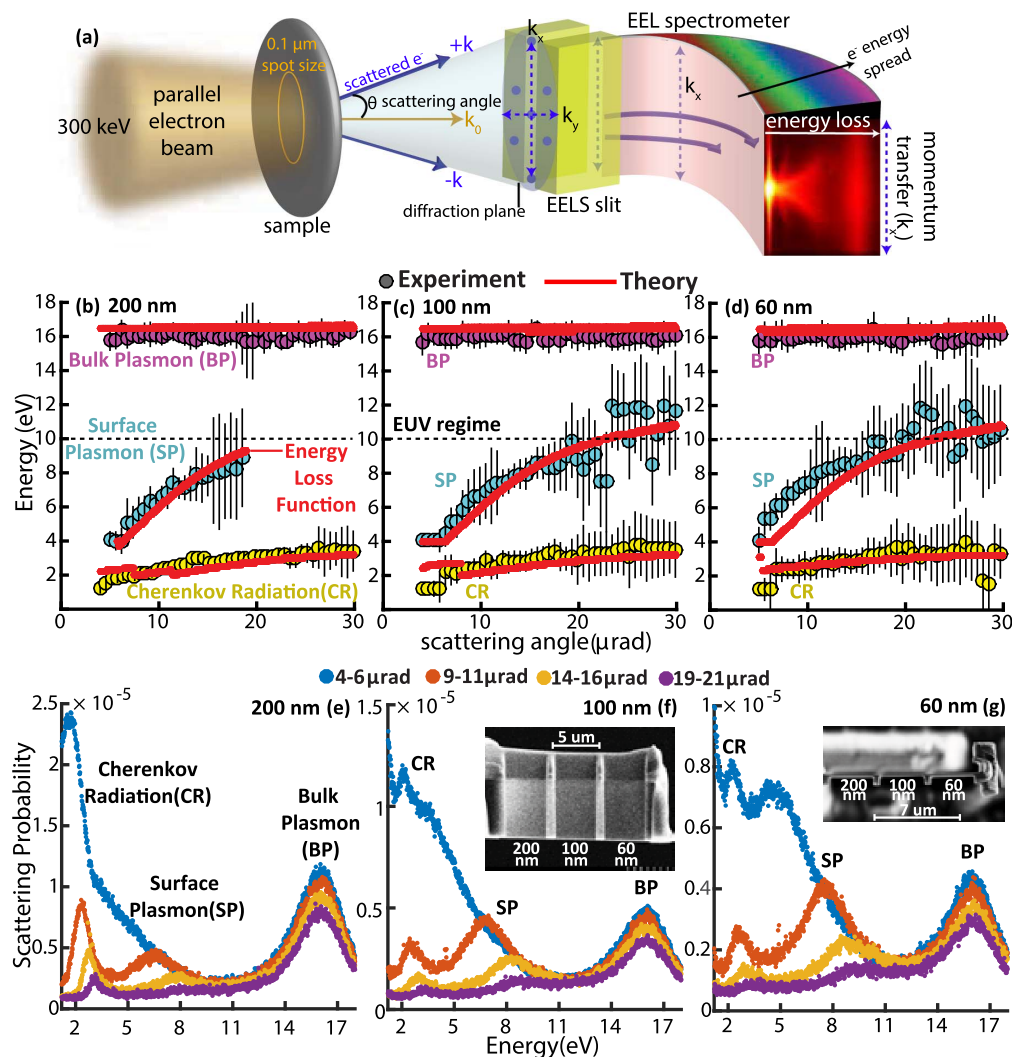
Fig. 2. EUV plasmons and CR in silicon measured with *k*-EELS. (a) Schematic showing the key components of the *k*-EELS technique for measuring the momentum-resolved photonic band structure of silicon. The *k*-EELS experiment was performed with a Hitachi HF-3300 TEM with a GIF Tridiem in *k*-EELS mode at 300 keV incident energy with parallel illumination resulting in a quantitative energy-momentum dispersion map of the excitations in the sample (details in Supplement 1). The photonic band structure of (b) 200 nm; (c) 100 nm; and (d) 60 nm thick silicon films measured with *k*-EELS (error bars show 95% confidence interval). All three films show evidence of the BP at ($\approx$16 eV) and the SP at ($\approx$4–11.5 eV) in the EUV as well as CR in the visible in the ($\approx$2–4 eV) region mapped to large scattering angles (large momentum with $k > 5 * k_0$). A good agreement to the macroscopic electrodynamic energy loss function (red line) is seen for all three thicknesses. (e), (f), and (g) show the electron scattering probability for the three excitations as measured by *k*-EELS integrated over the indicated scattering angles for the 200, 100, and 60 nm silicon films, respectively. Insets in (f) and (g) show scanning electron microscope images of the free-standing silicon films prepared via FIB milling and mounted to the TEM grid.

dispersive properties of the SPP would be hidden in traditional electron energy loss spectroscopy techniques but is captured here by *k*-EELS. The *k*-EELS measurements prove that the SPP of silicon can be probed to an entirely new region of the spectrum as compared to other plasmonic materials opening the door for a wide range of plasmonic applications in the EUV.

To prove conclusively that we are observing bulk and SPs in the measured data, we conduct simulations of the macroscopic electrodynamic electron energy loss function [25] in silicon for electrons normally incident to the sample. The measured data show a strong match with the theoretical calculations [red line in Figs. 2(b)–2(d)]. The energy loss function has been shown to be analogous to the photonic density of states [26,27] and is thus an excellent quantifier for probing photonic excitations. Slight deviations at small scattering angles of the experimental

SP peak from the predicted theoretical energy loss function in the 60 nm film is likely due to Ga+ implantation ($\approx$1–2 nm) during the FIB sample fabrication process and surface oxidation. Thinner samples, which are more sensitive to surface energy loss excitations, are more affected by such impurities along the sample surface. Recorded uncertainties (error bars) in the measured EUV plasmonic resonances increase at large scattering angles due to the decrease in probability of scattering (see Supplement 1 for details).

Figure 3 shows the ratio of the bulk and surface scattering probability scaling with momentum for silicon. Theoretical predictions reveal a k^{-3} dependence for BPs and k^{-2} scaling for SPs [24,26] (Fig. 3). The excellent agreement between theory and experiment (ratio = k^{-1}) allows us to unambiguously separate the contributions of bulk and SPs in silicon. We emphasize that this
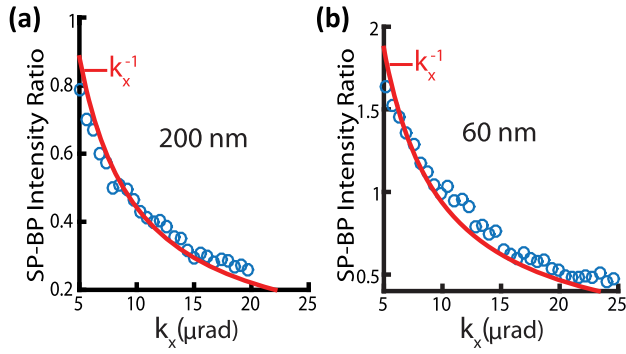
(a)

(b)

Fig. 3. *k*-EELS scattering intensity scaling with momentum (*k*) The experimental (blue circles) SP and the BP scattering peak intensity ratio is plotted as a function of k_x (scattering angle) for the (a) 200 nm and (b) 60 nm silicon films. In macroscopic electrodynamic electron energy loss theory, surface contributions (such as the SP) and bulk contributions (such as the BP) scale with momentum as k^{-3} and k^{-2}, respectively [24,26]. As a result, the *k*-space scaling of the ratio of the surface to bulk intensity goes as k^{-1}. This is evident from the red line in the figure. We can thus unambiguously separate the SPP and BP contributions using *k*-EELS.

scaling effect of the energy loss intensity with momentum can only be captured by *k*-EELS.

Finally, we explain the low energy branch in the visible range (1.5–4 eV) that is observed in the data. Through analytical simulations and electron energy loss function theory, we confirm that this branch is the visible-region CR in silicon. CR is EM radiation generated when a charged moving particle passes through a medium with a velocity greater than the phase velocity of light in the medium. It has been studied in multitudes of dielectrics in energy loss experiments [17,24,28–30] as well as in 2D materials [31] and metamaterials [32,33]. Conventional CR in dielectrics will only be generated if the electron velocity is larger than the phase velocity in the medium ($v_z \geq c/\sqrt{\epsilon}$). The threshold electron velocity to observe CR is thus defined as the phase velocity of light inside the medium ($v_{th} = c/\sqrt{\epsilon}$). The CR condition is satisfied in the visible region in silicon (where $\epsilon_{Si} > 1.64$; see Fig. S1) for the relativistic electrons used in our experiment. The CR peak and band structure in the 200, 100, and 60 nm silicon films between ≈2–4 eV (310–620 nm) in Fig. 2, respectively, is measured with *k*-EELS with an incident electron energy of 300 keV ($v_z = 0.78c$), well above the CR velocity threshold. Our results agree strongly with electron energy loss theory [red line in Figs. 2(b), 2(c), 2(d)] as well as previous studies [17,28,34]. We emphasize the striking fact that our observation of visible CR occurs in a 60 nm silicon thin film that is in the deep subwavelength nanophotonic regime. A detailed analysis of coherence properties of this visible CR will be undertaken in a future study. Additional details of CR in silicon films can be seen in Supplement 1.

3. PUSHING CR IN SILICON FROM THE VISIBLE TO THE EUV

We now discuss how the plasmonic properties of silicon can be exploited to design EUV radiation sources by pushing the Cherenkov emission into the EUV regime. We propose to use the plasmonic properties of silicon to design a new class of

high-energy (EUV) HMMs. Specifically, the multitude of applications possible with HMMs can now be expanded into the EUV, specifically the generation of a tunable, broadband, and TCR light source via electron excitation.

Interestingly, it has recently been shown that HMMs, a uniaxial metamaterial with a metallic response along one direction and a dielectric response along the orthogonal direction, can be used to eliminate the need for large velocity electrons for generating CR [35–37]. While on its own, silicon can only support conventional CR in the visible, its plasmonic properties in the DUV → EUV (Section 2) can be used to realize structures with hyperbolic behavior that generate TCR in this untapped region of the spectrum.

The novel TCR phenomena possible in HMMs can be determined by first considering the CR cone angle (θ_c) in uniaxial media:

$$\tan(\theta_c) = \sqrt{\left(\frac{v_z}{c}\right)^2 \epsilon_z - \frac{\epsilon_z}{\epsilon_x}}, \qquad (1)$$

where θ_c is the angle between the Cherenkov wave vector (k_c) and the axis of the electron trajectory [Fig. 4(a)], ϵ_x is the permittivity of the uniaxial structure in the planar direction, and ϵ_z is the permittivity parallel to the c axis (see Supplement 1 for details).

In the case of an HMM, we impose the following conditions on our permittivity for the orthogonal directions of the metallic and dielectric response: $\epsilon_z < 0$, $\epsilon_x > 0$ (type I HMM) and $\epsilon_z > 0$, $\epsilon_x < 0$ (type II HMM). The CR velocity threshold with the imposed HMM permittivity conditions can be determined by requiring real values of θ_c in Eq. (1):

$$v_z \leq c/\sqrt{\epsilon_x} \quad \text{Type I,} \qquad (2)$$

$$0 \leq v_z \leq c \quad \text{Type II.} \qquad (3)$$

We see that in the case of an HMM for the type I case, the electron velocity now has an upper limit. This is the exact opposite of a conventional isotropic dielectric, where a minimum velocity, i.e., lower limit, exists ($v_z \geq c/\sqrt{\epsilon}$). Furthermore, for the type II HMM, any electron velocity will generate CR (details in Supplement 1). These are the cases of TCR. Observe that if we consider a simple isotropic dielectric in Eq. (1) ($\epsilon_x = \epsilon_z \geq 0$), we retrieve the conventional CR limit ($v_z \geq c/\sqrt{\epsilon}$). Additionally, note that the conditions for the type I and type II CR velocity thresholds would be flipped for an electron traveling along the x direction, as was seen in [35].

Via harnessing silicon's unique EUV plasmonic properties (Section 2), novel EUV HMMs can be designed using widely used materials in a simple geometry such as a Si/SiO₂ multilayer stack. Figure 4(a) shows such a Si/SiO₂ multilayer structure whose permittivities in the effective medium limit (homogenized with Maxwell–Garnett theory; details in Supplement 1) possess both type I and type II hyperbolic behavior from the DUV to the EUV [Fig. 4(b)]. We envision that a practical realization of this structure would consist of approximately 16–20 alternating 8–10 nm layers of SiO₂ and crystalline Si. We strongly emphasize that our silicon-based metamaterial design is unique and is unrelated to previous approaches exploiting doped semiconductors [9,10] or alternate plasmonic media [7]. Also note
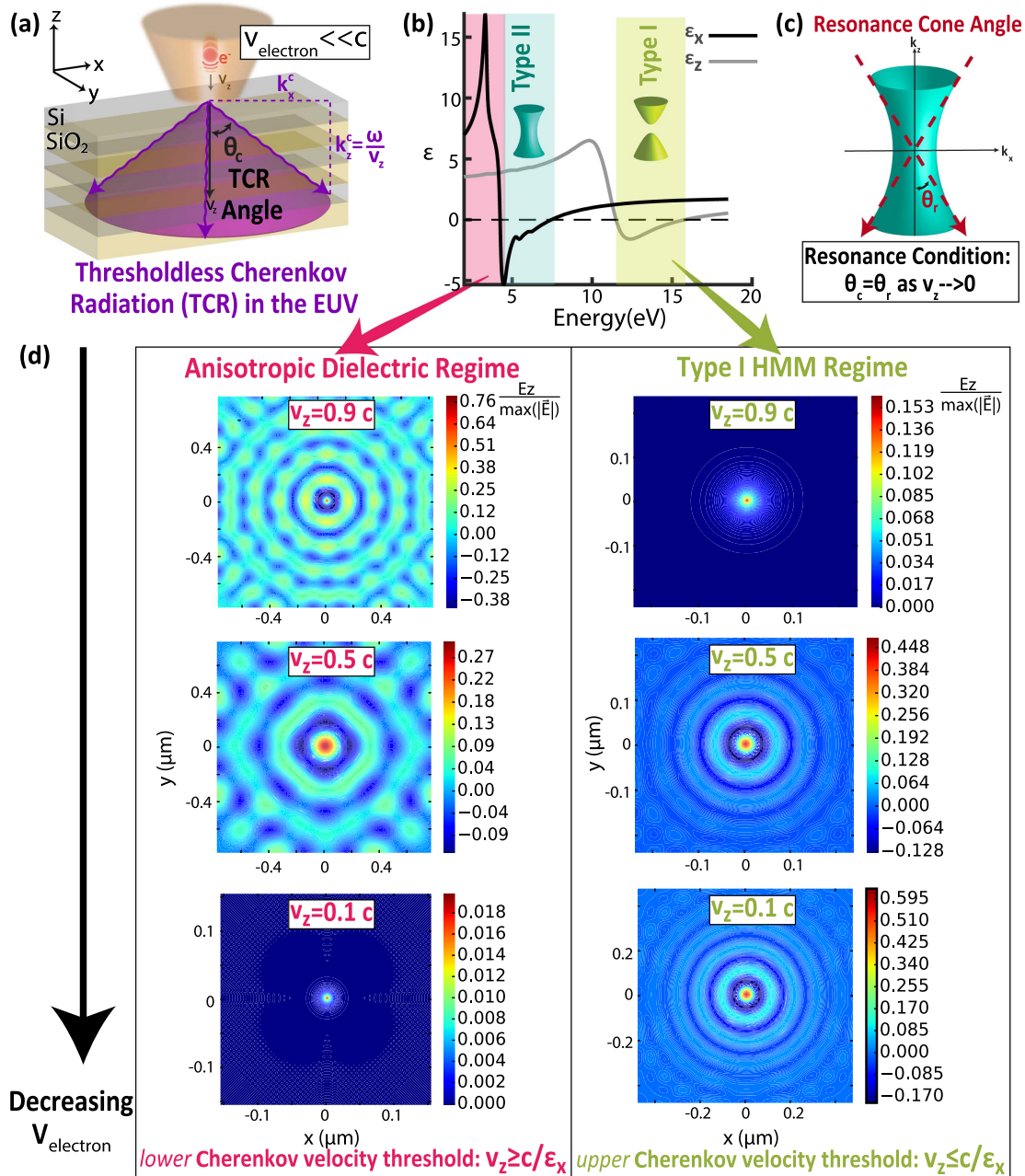
Fig. 4. TCR in the EUV. (a) Schematic of TCR ($v_z \ll c$) in the EUV excited in a HMM composed of a 100 nm thick Si/SiO$_2$ multilayer stack in the effective medium limit. k^c is the TCR wave vector and θ_c is the TCR cone angle. (b) Uniaxial effective medium permittivity at 0.35 metallic fill fraction for the Si/SiO$_2$ multilayer stack highlighting the regions of type I and type II behavior where TCR can be observed. (c) Type II ($\epsilon_x < 0$, $\epsilon_z > 0$) HMM isofrequency typology that supports TCR. In the ideal limit, the strongest TCR resonance occurs as $v_z \to 0$, where θ_c lies along the asymptotes of the hyperbola in k-space (defined by angle θ_r) (details in Supplement 1). (d) Normalized E_z fields in the x–y plane of CR in the dielectric and hyperbolic regimes of the Si/SiO$_2$ multilayer stack at different electron velocities in a lossless structure. Opposite trends are observed where the field strengths increase for the hyperbolic regime, while they are suppressed in the dielectric regime as the electron velocity decreases. The type I regime is seen to support TCR in the EUV ($\approx$11–15.5 eV).

that doped semiconductors cannot have plasmonic responses at high frequencies beyond the infrared region.

The hyperbolic regimes of the Si/SiO$_2$ multilayer stack give rise to the unique TCR excitation. This is clearly seen in Fig. 4(d), which shows the simulated CR fields in the dielectric and hyperbolic regimes of the Si/SiO$_2$ multilayer at different electron velocities. We observe in the type I regime that as the electron velocity decreases, the relative CR fields increase. This is the fundamental

characteristic of TCR and is the exact opposite trend seen in the dielectric regime, which supports conventional CR. CR in the hyperbolic regime can be seen down to electron velocities as low as $v_z = 0.001c$ in the effective medium limit; however, there is a fundamental trade-off between the velocity threshold reduction and the loss in the structure (see Supplement 1).

Note that the type I regime supports TCR in the EUV ($\approx$11–15.5 eV) for the Si/SiO$_2$ structure. This allows for a
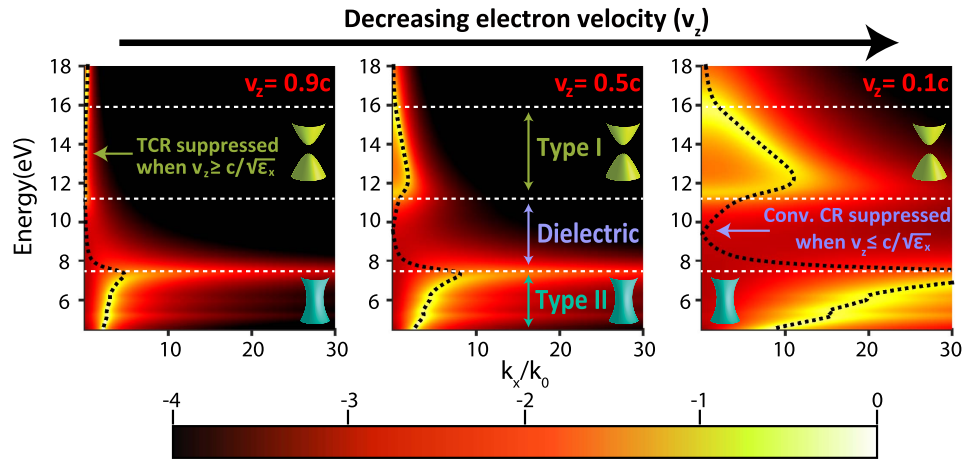
Fig. 5.   TCR dispersion from the DUV to the EUV. Simulation of the momentum-resolved electron scattering probability (calculated via the energy loss function) for the Si/SiO$_2$ structure described in Fig. 4 for different incident electron velocities. The simulations are performed in the effective medium (homogenized) low-loss limit. The dashed black line shows the analytical CR dispersion in a uniaxial metamaterial described in Eq. (S1) of Supplement 1. TCR is clearly observed in the type I and type II HMM regimes, where the scattering probability increases with decreasing electron velocity. Note that the type I region has an upper threshold when $v_z \geq c/\sqrt{\epsilon_x}$ and is suppressed at $v_z = 0.9c$. The type II region has no velocity threshold. Additionally, the TCR dispersion extends to larger wave vectors as the velocity decreases, as it is approaching the resonance condition described in Fig. 4(b), where infinitely large wave vectors are supported in the structure and $v_{\text{phase}} = \omega/k \to 0$.

potential EUV source from low-energy electrons not possible with conventional CR. Additionally, the hyperbolic regions can be shifted in energy space by adjusting the silicon (metallic) fill fraction, allowing for a TCR excitation that is highly tunable and considerably broadband. This is in contrast to other high-energy CR sources that are narrowband, nontunable, and are subject to the conventional CR threshold [38,39].

The origin of the TCR phenomenon is due to the unique hyperbolic topology of the HMM isofrequency surface [Fig. 4(c)]. Note that the phase velocity in the medium approaches 0 at the asymptotes ($v_{\text{phase}} = \omega/k \to 0$). As explained previously, the threshold velocity of CR can be connected to the phase velocity of light in the medium $v_{\text{th}} = v_{\text{phase}}$. In the limit of a vanishing electron velocity $v_z \to 0$, the Cherenkov wave vector can lie along the asymptotes of the hyperbola ($\theta_c = \theta_r$), where infinitely large wave vectors can be supported by the structure in the ideal limit (see Supplement 1). Consequently, the threshold velocity also vanishes ($v_{\text{th}} \to 0$) in hyperbolic media.

This point is further clarified in Fig. 5, which plots the momentum-resolved electron scattering probability for CR in the Si/SiO$_2$ multilayer stack for different electron velocities (as calculated from the energy loss function [25]). Our numerical simulation uses effective medium theory. We observe that as the velocity decreases, the scattering probability in the hyperbolic regions increases. There is an excellent agreement between the results of our numerical simulation and analytical theory of CR, denoted by the black dashed line. Additionally, this analytic TCR dispersion [Eq. (S1) of Supplement 1] highlights that the TCR extends to larger wave vectors as the electron velocity decreases (dashed black line). This is due to the fact that we are approaching closer to the resonance condition [Fig. 4(c)], where infinitely large wave vectors are supported by the structure. We emphasize that the fundamental limit to how low the velocity can reach in practice will be determined by absorption and the finite unit cell size (see Supplement 1). These ideas will be elaborated on in a future publication.

4. CONCLUSION

In conclusion, we experimentally demonstrate the generation of EUV plasmons supported by silicon with energies twice as large as those seen with aluminum via momentum-resolved electron energy loss spectroscopy. k-EELS is the ideal tool to observe such high-energy excitations while simultaneously mapping the photonic band structure of plasmonic excitations to large wave vectors not possible with conventional electron energy loss spectroscopy techniques. Our experimental observations are rigorously validated using macroscopic electrodynamic simulations of k-EELS and also first-principles DFT. Additionally, we proposed a simple Si/SiO$_2$ multilayer stack with a hyperbolic isofrequency response that can generate tunable and broadband TCR in the EUV by harnessing silicon's unique EUV plasmonic properties. This can lead to applications in EUV waveguides/metamaterials/nanoantennas/hybrid MEMS based on silicon, EUV light sources generated with low energy excitations, detectors for observation of nonrelativistic particles, and the development of TCR free-electron lasers [37].

See Supplement 1 for supporting content.

REFERENCES

1. A. H. Atabaki, S. Moazeni, F. Pavanello, H. Gevorgyan, J. Notaros, L. Alloatti, M. T. Wade, C. Sun, S. A. Kruger, H. Meng, K. A. Qubaisi,

I. Wang, B. Zhang, A. Khilo, C. V. Baiocco, M. A. Popović, V. M. Stojanović, and R. J. Ram, "Integrating photonics with silicon nanoelectronics for the next generation of systems on a chip," Nature **556**, 349–354 (2018).

2. F. Priolo, T. Gregorkiewicz, M. Galli, and T. F. Krauss, "Silicon nanostructures for photonics and photovoltaics," Nat. Nanotechnol. **9**, 19–32 (2014).

3. E. Arbabi, A. Arbabi, S. M. Kamali, Y. Horie, M. Faraji-Dana, and A. Faraon, "MEMS-tunable dielectric metasurface lens," Nat. Commun. **9**, 812 (2018).

4. S. Jahani, S. Kim, J. Atkinson, J. C. Wirth, F. Kalhor, A. A. Noman, W. D. Newman, P. Shekhar, K. Han, V. Van, R. G. DeCorby, L. Chrostowski, M. Qi, and Z. Jacob, "Controlling evanescent waves using silicon photonic all-dielectric metamaterials for dense integration," Nat. Commun. **9**, 1893 (2018).

5. S. Jahani and Z. Jacob, "All-dielectric metamaterials," Nat. Nanotechnol. **11**, 23–36 (2016).

6. I. Staude and J. Schilling, "Metamaterial-inspired silicon nanophotonics," Nat. Photonics **11**, 274–284 (2017).

7. P. West, S. Ishii, G. Naik, N. Emani, V. Shalaev, and A. Boltasseva, "Searching for better plasmonic materials," Laser Photon. Rev. **4**, 795–808 (2010).

8. L. Ju, B. Geng, J. Horng, C. Girit, M. Martin, Z. Hao, H. A. Bechtel, X. Liang, A. Zettl, Y. R. Shen, and F. Wang, "Graphene plasmonics for tunable terahertz metamaterials," Nat. Nanotechnol. **6**, 630–634 (2011).

9. A. J. Hoffman, L. Alekseyev, S. S. Howard, K. J. Franz, D. Wasserman, V. A. Podolskiy, E. E. Narimanov, D. L. Sivco, and C. Gmachl, "Negative refraction in semiconductor metamaterials," Nat. Mater. **6**, 946–950 (2007).

10. P. Shekhar and Z. Jacob, "Strong coupling in hyperbolic metamaterials," Phys. Rev. B **90**, 045313 (2014).

11. D. K. Gramotnev and S. I. Bozhevolnyi, "Plasmonics beyond the diffraction limit," Nat. Photonics **4**, 83–91 (2010).

12. I. Gryczynski, J. Malicka, Z. Gryczynski, K. Nowaczyk, and J. R. Lakowicz, "Ultraviolet surface plasmon-coupled emission using thin aluminum films," Anal. Chem. **76**, 4076–4081 (2004).

13. M. W. Knight, L. Liu, Y. Wang, L. Brown, S. Mukherjee, N. S. King, H. O. Everitt, P. Nordlander, and N. J. Halas, "Aluminum plasmonic nanoantennas," Nano Lett. **12**, 6000–6004 (2012).

14. A. Ono, M. Kikawada, R. Akimoto, W. Inami, and Y. Kawata, "Fluorescence enhancement with deep-ultraviolet surface plasmon excitation," Opt. Express **21**, 17447–17453 (2013).

15. Z. Liu, J. M. Steele, W. Srituravanich, Y. Pikus, C. Sun, and X. Zhang, "Focusing surface plasmons with a plasmonic lens," Nano Lett. **5**, 1726–1729 (2005).

16. J. A. Scholl, A. L. Koh, and J. A. Dionne, "Quantum plasmon resonances of individual metallic nanoparticles," Nature **483**, 421–427 (2012).

17. C. H. Chen, J. Silcox, and R. Vincent, "Electron-energy losses in silicon: bulk and surface plasmons and Čerenkov radiation," Phys. Rev. B **12**, 64–71 (1975).

18. E. D. Palik, *Handbook of Optical Constants of Solids* (Academic, 1998).

19. G. Kresse and J. Furthmüller, "Efficient iterative schemes for ab initio total-energy calculations using a plane-wave basis set," Phys. Rev. B **54**, 11169–11186 (1996).

20. H. R. Philipp and H. Ehrenreich, "Optical properties of semiconductors," Phys. Rev. **129**, 1550–1560 (1963).

21. T. Sasaki and K. Ishiguro, "Optical constants of silicon in the extreme ultraviolet region," Phys. Rev. **127**, 1091–1092 (1962).

22. P. Lautenschlager, M. Garriga, L. Vina, and M. Cardona, "Temperature dependence of the dielectric function and interband critical points in silicon," Phys. Rev. B **36**, 4821–4830 (1987).

23. F. J. Garcia de Abajo, "Optical excitations in electron microscopy," Rev. Mod. Phys. **82**, 209–275 (2010).

24. R. Egerton, *Electron Energy-Loss Spectroscopy in the Electron Microscope* (Springer, 2011).

25. C. H. Chen and J. Silcox, "Calculations of the electron-energy-loss probability in thin uniaxial crystals at oblique incidence," Phys. Rev. B **20**, 3605–3614 (1979).

26. P. Shekhar, M. Malac, V. Gaind, N. Dalili, A. Meldrum, and Z. Jacob, "Momentum-resolved electron energy loss spectroscopy for mapping the photonic density of states," ACS Photon. **4**, 1009–1014 (2017).

27. F. J. Garcia de Abajo and M. Kociak, "Probing the photonic local density of states with electron energy loss spectroscopy," Phys. Rev. Lett. **100**, 106804 (2008).

28. A. Yurtsever, M. Couillard, and D. A. Muller, "Formation of guided Cherenkov radiation in silicon-based nanocomposites," Phys. Rev. Lett. **100**, 217402 (2008).

29. F. J. García de Abajo and A. Howie, "Retarded field calculation of electron energy loss in inhomogeneous dielectrics," Phys. Rev. B **65**, 115418 (2002).

30. I. Frank and I. Tamm, "Coherent visible radiation of fast electrons passing through matter," in *Selected Papers* (Springer, 1991), pp. 29–35.

31. I. Kaminer, Y. T. Katan, H. Buljan, Y. Shen, O. Ilic, J. J. López, L. J. Wong, J. D. Joannopoulos, and M. Soljačič, "Efficient plasmonic emission by the quantum Čerenkov effect from hot carriers in graphene," Nat. Commun. **7**, 11880 (2016).

32. G. Adamo, K. F. MacDonald, Y. H. Fu, C.-M. Wang, D. P. Tsai, F. J. García de Abajo, and N. I. Zheludev, "Light well: a tunable free-electron light source on a chip," Phys. Rev. Lett. **103**, 113901 (2009).

33. V. Ginis, J. Danckaert, I. Veretennicoff, and P. Tassin, "Controlling Cherenkov radiation with transformation-optical metamaterials," Phys. Rev. Lett. **113**, 167402 (2014).

34. R. Erni and N. D. Browning, "The impact of surface and retardation losses on valence electron energy-loss spectroscopy," Ultramicroscopy **108**, 84–99 (2008).

35. F. Liu, L. Xiao, Y. Ye, M. Wang, K. Cui, X. Feng, W. Zhang, and Y. Huang, "Integrated Cherenkov radiation emitter eliminating the electron velocity threshold," Nat. Photonics **11**, 289–292 (2017).

36. D. E. Fernandes, S. I. Maslovski, and M. G. Silveirinha, "Cherenkov emission in a nanowire material," Phys. Rev. B **85**, 155107 (2012).

37. J.-K. So, J.-H. Won, M. A. Sattorov, S.-H. Bak, K.-H. Jang, G.-S. Park, D. S. Kim, and F. J. Garcia-Vidal, "Cherenkov radiation in metallic metamaterials," Appl. Phys. Lett. **97**, 151107 (2010).

38. W. Knulst, M. J. van der Wiel, O. J. Luiten, and J. Verhoeven, "High-brightness, narrowband, and compact soft x-ray Cherenkov sources in the water window," Appl. Phys. Lett. **83**, 4050–4052 (2003).

39. W. Knulst, O. J. Luiten, M. J. van der Wiel, and J. Verhoeven, "Observation of narrow-band Si L-edge Čerenkov radiation generated by 5 MeV electrons," Appl. Phys. Lett. **79**, 2999–3001 (2001).